



Photographic study and modeling of critical heat flux in horizontal flow boiling with inlet vapor void

Chirag R. Kharangate^a, Issam Mudawar^{a,*}, Mohammad M. Hasan^b

^aBoiling and Two-phase Flow Laboratory, School of Mechanical Engineering, Purdue University, 585 Purdue Mall, West Lafayette, IN 47907-2088, USA

^bNASA Glenn Research Center, 21000 Brookpark Road, Cleveland, OH 44135, USA

ARTICLE INFO

Article history:

Received 24 June 2011

Received in revised form 28 February 2012

Accepted 28 February 2012

Available online 20 April 2012

Keywords:

Flow boiling

Two-phase pressure drop

Critical heat flux (CHF)

ABSTRACT

This study explores the mechanism of flow boiling critical heat flux (CHF) in a 2.5 mm × 5 mm horizontal channel that is heated along its bottom 2.5 mm wall. Using FC-72 as working fluid, experiments were performed with mass velocities ranging from 185–1600 kg/m²s. A key objective of this study is to assess the influence of inlet vapor void on CHF. This influence is examined with the aid of high-speed video motion analysis of interfacial features at heat fluxes up to CHF as well as during the CHF transient. The flow is observed to enter the heated portion of the channel separated into two layers, with vapor residing above liquid. Just prior to CHF, a third vapor layer begins to develop at the leading edge of the heated wall beneath the liquid layer. Because of buoyancy effects and mixing between the three layers, the flow is less discernible in the downstream region of the heated wall, especially at high mass velocities. The observed behavior is used to construct a new separated three-layer model that facilitates the prediction of individual layer velocities and thicknesses. Combining the predictions of the new three-layer model with the interfacial lift-off CHF model provides good CHF predictions for all mass velocities, evidenced by a MAE of 11.63%.

© 2012 Elsevier Ltd. All rights reserved.

1. Introduction

Flow boiling is widely used in applications demanding the removal of high heat fluxes while maintaining low surface temperatures. These include nuclear reactor cores, lasers, advanced microprocessors and hybrid vehicle power electronics [1]. A primary design goal in these applications is to ensure coolant operating conditions that yield critical heat flux (CHF) values safely above the dissipated heat flux. For applications where the heat dissipation is heat-flux controlled, exceeding CHF can potentially lead to catastrophic failure of the device or system because of the ensuing uncontrolled rise in surface temperature.

When implemented in most of these applications, the flow is maintained mostly in subcooled state to capitalize upon the coolant's ability to cool surfaces by sensible heat absorption in addition to its latent heat of vaporization. However, maintaining subcooled conditions is not always possible in a two-phase cooling system. For example, a single two-phase loop may be used to cool an array of heat dissipating modules in series, in which case the incoming subcooled liquid gradually loses sensible heat as it flows through the system. So, even if upstream modules can capitalize

upon the high sensible heat content of the coolant, downstream modules may contend with only saturated flow boiling. For the latter, the coolant may enter the modules with a finite vapor void fraction. It is therefore very important for this cooling scenario to be able to predict CHF for saturated flow boiling with appreciable vapor content. Exploring such operating conditions for horizontal flow is the primary goal of the present study.

1.1. Flow boiling critical heat flux

Numerous studies have been published over the years that address horizontal flow boiling and CHF. In general, upward facing heated walls are preferred for horizontal flow to take advantage of the buoyancy forces in helping remove vapor from the heated wall and replenish the wall with bulk liquid, two mechanisms that are vital for sustaining nucleate boiling and delay the formation of the vapor blanket known to precede CHF. These benefits are especially important for low velocity flows, where weak liquid drag magnifies the influence of buoyancy in a horizontal channel.

Identifying the trigger mechanism for CHF in flow boiling has been the subject of intense research for many decades. Four different categories of models have been suggested, *boundary layer separation*, *bubble crowding*, *sublayer dryout*, and *interfacial lift-off*. The boundary layer separation model is based on the assumption that the near-wall liquid velocity gradient becomes vanishingly small

* Corresponding author. Tel.: +1 765 494 5705; fax: +1 765 494 0539.

E-mail address: mudawar@ecn.purdue.edu (I. Mudawar).

URL: <https://engineering.purdue.edu/BTFPL> (I. Mudawar).

1.2. Two-phase pressure drop

Pressure drop for flow boiling with saturated inlet conditions and finite vapor void is typically predicted using the Homogeneous Equilibrium Model (HEM) or any number of Separated Flow Models (SFM) [16,17]. HEM is based on the assumption that velocities of liquid and vapor phases are both equal and uniform across the flow channel's cross section, while SFMs permit differences between the phase velocities. Most recent SFMs of the two-phase frictional pressure drop are based on the formulation by Lockhart and Martinelli [18] originally developed for isothermal two-component mixtures. Martinelli and Nelson [19] developed a method for determining the accelerational component of two-phase pressure drop. To predict the two-phase frictional pressure drop, Thom [20] formulated two-phase friction multiplier relations for steam-water. Baroczy [21] formulated an empirical two-phase friction multiplier in terms of mass velocity, quality and physical properties for liquid metals and refrigerants. Chisholm [22] modified the original frictional pressure drop model of Lockhart and Martinelli with an interfacial shear term. Friedel [23] later provided updated correlations for two-phase friction multipliers using a large data base he amassed from different sources.

An alternative approach to predicting two-phase pressure drop for separated flows is to use the control volume method, where conservation laws are applied to control volumes encompassing the liquid and vapor phases separately, and later combined for the two-phase mixture. The control volume method proved highly accurate in predicting two-phase pressure drop for vertical separated flow along short [8] and long heated walls [9,10,24–27].

1.3. Study objectives

The present study will explore pressure drop and CHF associated with flow boiling in a rectangular horizontal channel with an upward-facing heated wall. The focus of this study is on saturated flow at the inlet with a finite void fraction, conditions that prevail in downstream heat-dissipating modules when a number of modules are cooled in series using the same flow loop. High-speed video imaging techniques are used to explore vapor coalescence, especially near CHF. Pressure drop data will be compared to predictions of previous models as well as a new control-volume-based model. CHF data will be compared against the predictions of popular saturated flow boiling correlations and the Interfacial Lift-off Model.

2. Experimental methods

2.1. Flow boiling test module

The flow-boiling module used in this study consists of two plates of polycarbonate (Lexan) pressed together between two outer aluminum plates using a series of bolts. As shown in Fig. 1(a), a $2.5 \text{ mm} \times 5 \text{ mm}$ rectangular flow channel is milled into the underside of the top plastic plate. The heated wall consists of a 0.56-mm-thick, 101.6-mm-long copper plate that is heated by a series of thick-film resistors. The heated wall is attached into a rectangular groove in the flow channel's bottom plastic plate. To prevent leaks, a flexible Teflon cord is inserted into a shallow o-ring groove in the upper surface of the bottom plastic plate. A honeycomb insert is placed at the channel inlet to straighten the flow and break up any large eddies. A channel entry length 106 times the hydraulic diameter ensures that liquid flow becomes fully developed upstream of the heated wall of the channel.

Fig. 1(b) shows the heated wall assembly consisting of six thick-film resistors that are soldered to the underside of the copper plate. Each resistor is 16.1 mm long by 4.0 mm wide and has a resistance of 188Ω . Five thermocouples are inserted into shallow holes in the copper plate along the centerline between the resistors. Uniform heat flux along the heated wall is ensured by both equal electrical resistance of the six resistors and by connecting the six resistors in parallel and using the same variable voltage power source. The thickness of the copper heated wall is chosen carefully to achieve two requirements simultaneously; details concerning these requirements are provided in [10]. Since very thin walls can induce premature CHF, the copper plate thickness is set greater than the 'asymptotic thickness' at which CHF becomes insensitive to the wall thickness. On the other hand, fast thermal response is achieved by avoiding a very large wall thickness. Using a copper thickness of 0.56 mm allows the wall to reach steady-state temperature between power increments in less than 5 s. These two requirements are based on the need to use the present flow boiling test module in parabolic flight experiments, where steady-state thermal response must be achieved within the 23 s microgravity duration of a single parabola. While performing parabolic flight experiments is beyond the scope of the present study, meeting those two requirements ensures accurate CHF measurement while allowing a complete boiling curve to be measured in a relatively short period of time.

2.2. Fluid conditioning loop

The desired operating conditions at the inlet to the flow boiling module are achieved with the aid of a compact two-phase flow

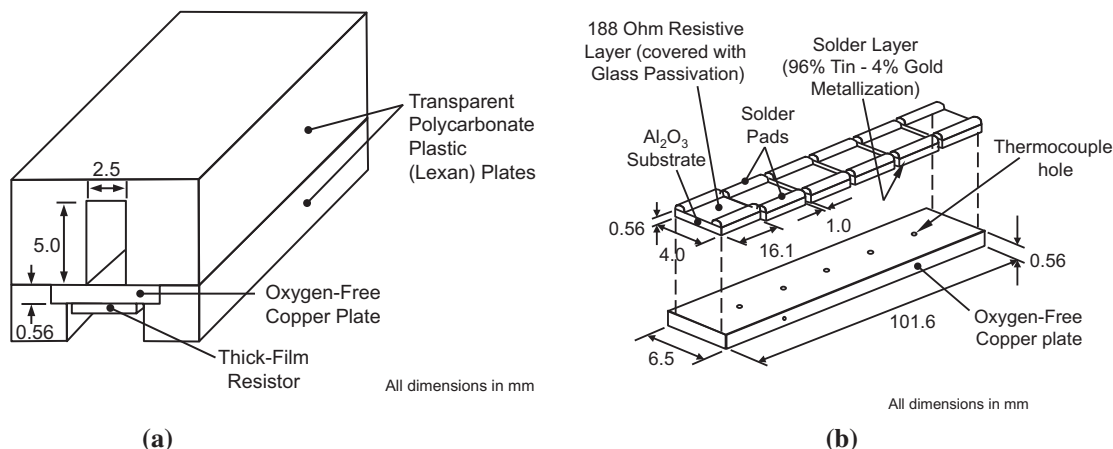


Fig. 1. (a) Flow channel assembly. (b) Construction of heated wall.

loop depicted schematically in Fig. 2(a). FC-72 is the working fluid used throughout the study. A detachable accessory to the two-phase loop is used to deaerate the FC-72 before performing a series of tests. In the main loop, the FC-72 is circulated with the aid of a variable speed pump. Exiting the pump, the flow is passed through a regulating valve followed by a filter, turbine flow meter, and two in-line electrical heaters, before entering the flow boiling module. The first in-line heater is used to fine-tune the liquid temperature but maintain single-phase liquid flow, while the second in-line heater is intended to achieve saturated flow with a finite void fraction at the inlet to the flow boiling module. With this arrangement, the flow quality at the inlet to the flow boiling module could be determined from measurements of power input to the second in-line heater as well as temperature and pressure measurements both upstream and downstream of the same heater. Exiting the flow boiling module, the two-phase mixture is routed to a condenser to convert the two-phase mixture to liquid state. A nitrogen-pressurized accumulator between the condenser and pump both compensates for any expansion or contraction of the working fluid throughout the loop as well as provides a stable reference pressure point for the loop's operation. Metal bellows inside the accumulator help manage any FC-72 volume changes in the loop.

2.3. Instrumentation and measurement accuracy

An array of instruments is used to measure power and fluid conditions throughout the flow loop. The temperature of the heated wall of the flow boiling module is measured by a series of five equidistant type-K thermocouples that are inserted into the copper wall as described earlier. Two additional thermocouples are placed just upstream and downstream of the heated wall. Pressure transducers are also connected to taps in the flow boiling module 13 mm upstream and downstream of the heated wall. The wall heat flux is determined by dividing the total electrical power input to the thick film resistors by the wetted area of the copper wall. The power input is measured by a wattmeter. Another wattmeter is used to measure power input to the second in-line heater. A thermocouple and a pressure transducer are used to measure temperature and pressure, respectively, at the inlet to the second in-line heater. The flow rate is measured by a turbine flow meter.

Accuracies of the flow rate, pressure, and heat flux measurements are estimated at 2.3%, 0.01%, and 0.2%, respectively. The fluid and wall temperatures are measured with thermocouples having an uncertainty of 0.3°C.

The entire apparatus, including the flow loop components, power and instrumentation cabinets and data acquisition system, is mounted onto a rigid extruded aluminum frame as shown in Fig. 2(b).

2.4. Flow visualization and void fraction determination

A Photron Fastcam Ultima APX camera system with a shutter speed of 1/20,000 is used for visualization of the boiling flow along the heated portion of the flow channel. A Nikon Micro-Nikkor 105 mm f/8D autofocus lens provides the high magnification required to capture interfacial features of interest. The camera is positioned in a side-view orientation normal to the side of the flow channel. The flow is backlit with a light source, with a semi-opaque sheet placed in between to soften and diffuse the incoming light.

As illustrated in Fig. 3(a), the flow visualization study targets three regions of the heated portion of the flow channel, inlet, middle and exit, each spanning 20 mm. Together, the three regions cover nearly 60% of the heated length. While images corresponding to the individual regions are sometimes smaller than 20 mm wide, all images presented in this paper for the inlet region include the upstream edge of the heated length, those for the middle region are centered at the middle of the heated length, and the exit region images include the downstream edge of the heated length.

Determining the void fraction is possible only when the vapor and liquid phases are clearly separated and also span the entire width of the flow channel. This is possible only for mass velocities of $G = 185\text{--}800 \text{ kg/m}^2\text{s}$. A high mass velocities, a combination of interfacial waviness, phase mixing, bubble entrainment in the liquid phase, and droplet entrainment in the vapor phase precludes accurate determination of the void fraction. When operating conditions are favorable, a systematic procedure is adopted for void fraction determination. Strong contrast between the separated liquid and vapor is used advantageously for this purpose. The captured images consist of 256 levels of gray scale. Image correction and adjustment of brightness and contrast shows the vapor and liquid phases clearly separated from one another. To calculate the void fraction, this technique is applied to a control volume of length $\Delta z = 3 \text{ mm}$ within the captured region spanning the entire height of the flow channel above the heated wall. Image analysis software is used to calculate the thickness of the vapor layer in pixels. The void fraction is calculated as the number of vapor pixels divided by the number of pixels corresponding to the entire height of the flow channel. This calculation procedure is applied to many

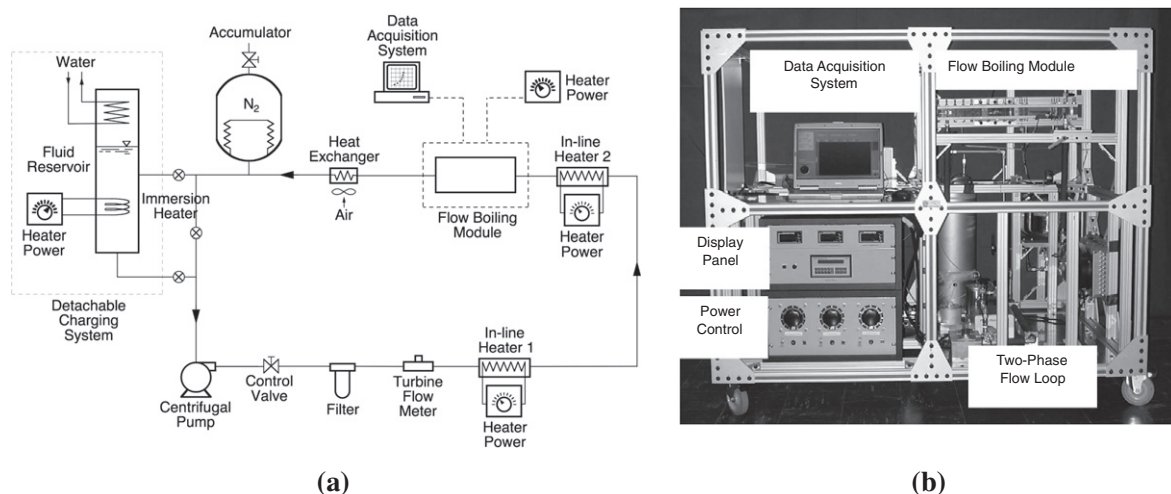


Fig. 2. (a) Schematic of two-phase loop. (b) Photo of test facility.

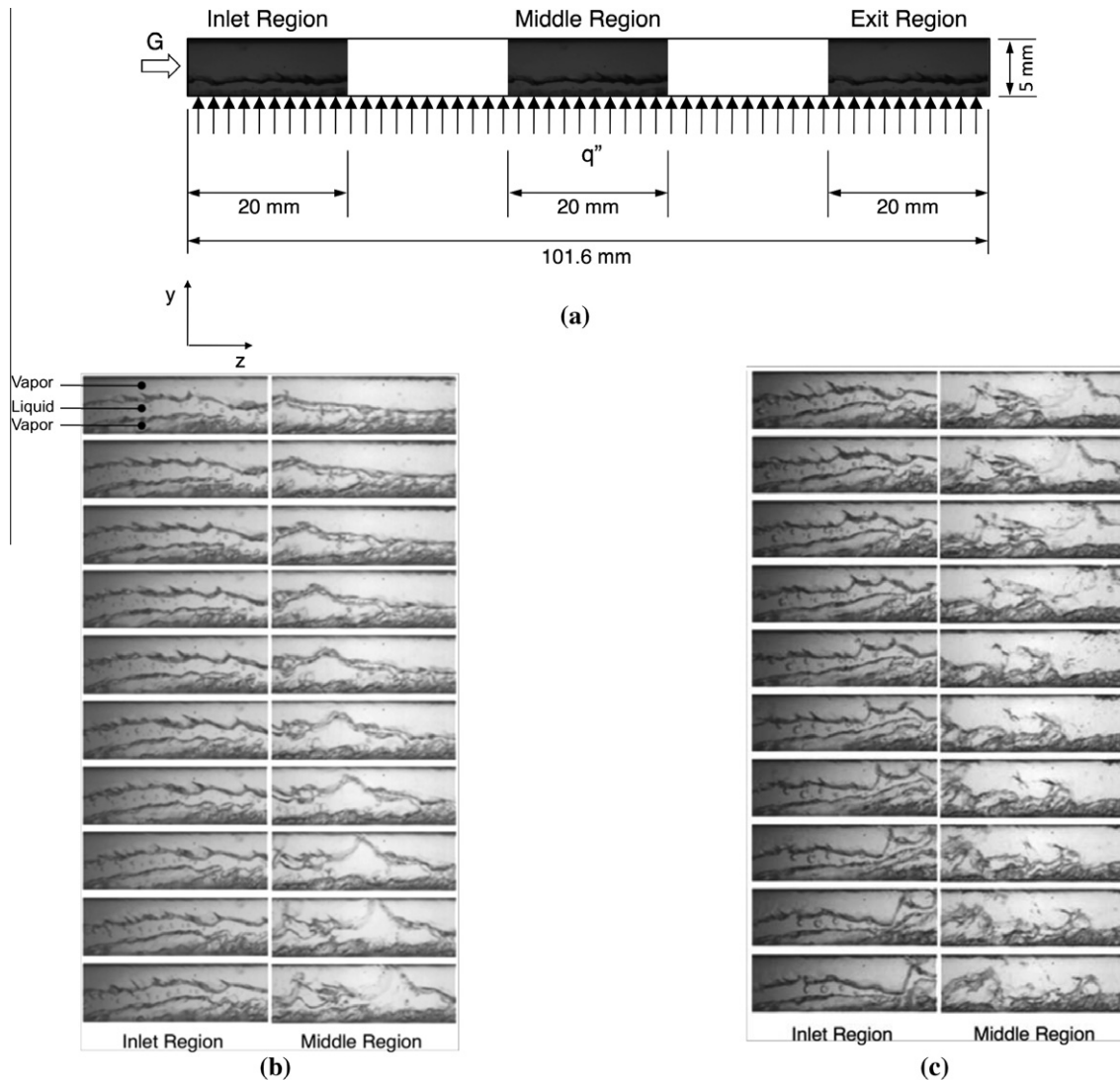


Fig. 3. (a) Inlet, middle and exit regions of heated portion of flow channel used for video capture, and sequential images of inlet and middle regions for $G = 335 \text{ kg/m}^2\text{s}$, $x_i = 0.0369$, $\alpha_i = 0.54$: (b) images 1–10 and (c) images 11–20.

thousands of images in a video file. Typically, images are recorded at 4000–8000 frames per second, and the camera recording time is limited to 1.024 s. Therefore, this procedure is repeated for 4–5 sets of images taken at different times. Void fraction estimates for the different times are typically within only $\pm 2\%$ of the mean value.

Other than optical limitations due to the camera, error associated with the void fraction determination comes in two main forms. First, the method used assumes that the flow is two-dimensional, that is, the vapor formation extends uninterrupted along the camera's viewing direction. This error is minimized by the short width (2.5 mm) of the rectangular flow channel. Second, this method could not account for minute bubbles that are entrained in the liquid layer or liquid droplets entrained in the vapor layer.

3. Flow visualization results

Fig. 3(b) and (c) show video images of the inlet and middle regions of the heated portion of the channel just prior to CHF, designated as CHF-in the present study. **Fig. 3(b)** shows for each region a sequence of ten consecutive video images for each region; **Fig. 3(c)**

shows the ten consecutive images that follow. The time elapsed between consecutive frames is 1.024/1024 s. Because of the lack of phase separation in the downstream region, images for this region could not be used for void fraction determination and are not shown in **Fig. 3**. Both **Fig. 3(b)** and (c) depict a unique three-layer formation in the inlet region. Images of the middle region show signs of mixing of the phases that leads to the aforementioned highly mixed flow in the downstream region. The two-phase flow arrives at the leading edge of the heated wall separated into two layers, with the vapor residing above the liquid due to buoyancy. A third vapor layer begins to evolve immediately at the leading edge of the heated wall. There is evidence of liquid at the wall beneath the lower vapor layer, providing localized cooling to the wall. Image sequences captured at different times show temporal variations in the vapor layer's shape and thickness due to waviness in the two interfaces between the three layers. In the inlet region, there is axial thinning of the lower separated vapor layer, bringing the middle separated liquid layer closer to the wall.

Fig. 3(b) and (c) show the upstream lower separated vapor layer becomes even thinner and is confined to the wall, perhaps mixing with the liquid layer. The vapor layer thinning is

attributed to the axial increase in mean flow velocity causing an increase in shear between the three layers. There are signs of mixing between the lower vapor layer and middle liquid layer because of buoyancy effects. This effect is more pronounced in the downstream region.

Fig. 4(a) depicts flow development for the inlet region with increasing heat flux up to 95% CHF. Initially, with no heat added, the flow consists of two clearly separated layers, with the vapor residing above the liquid due to buoyancy. At 50% CHF, bubbles can be seen forming at the wall then being entrained into the liquid layer or sliding along the wall; the flow consists essentially of a clearly separated vapor layer above a bubbly flow liquid layer. The three-layer flow becomes well developed at 95% CHF as bubble coalescence and axial growth of oblong bubbles culminates in the formation of a fairly continuous wavy vapor layer at the wall.

Fig. 4(b) shows, for two mass velocities, the flow behavior in the inlet, middle and exit regions at 95% CHF. Notice how, for each mass velocity, the three layers are clearly separated in the inlet region, while, for the middle region, the lower vapor layer is quite thin and appears to mix into the middle liquid layer, resulting in a seemingly two-layer flow. This behavior continues for the exit region, albeit with a much thinner mixed wall layer, caused by the increased mean flow velocity. As indicated earlier, buoyancy tends to mix the two lower layers as the flow reaches the middle region. Fig. 4(b) shows the lower mass velocity accentuates the buoyancy effects.

Fig. 5(a) and (b) shows images of the boiling flow in the exit region at 95% CHF (CHF-) and during the CHF transient (while wall temperatures begin to increase unsteadily) for $G = 335$ and $650 \text{ kg/m}^2\text{s}$, respectively. Using the same flow boiling module used in the present study, Zhang et al. [9] previously showed that, with zero vapor void at the inlet, a wavy vapor layer forms along the heated wall at CHF-. The wall could still be cooled by liquid from the bulk region through wetting fronts, troughs where the vapor layer interface makes contact with the wall. CHF ultimately occurs when intense boiling in the wettings fronts causes the vapor layer interface to separate fully from the wall, preventing any further liquid access to the wall. Fig. 5(a) and (b) show how the strong shear forces in the present study, which are the result of the relatively large vapor void, greatly decrease the thickness of the wall vapor layer, making any identification of near-wall effects quite elusive.

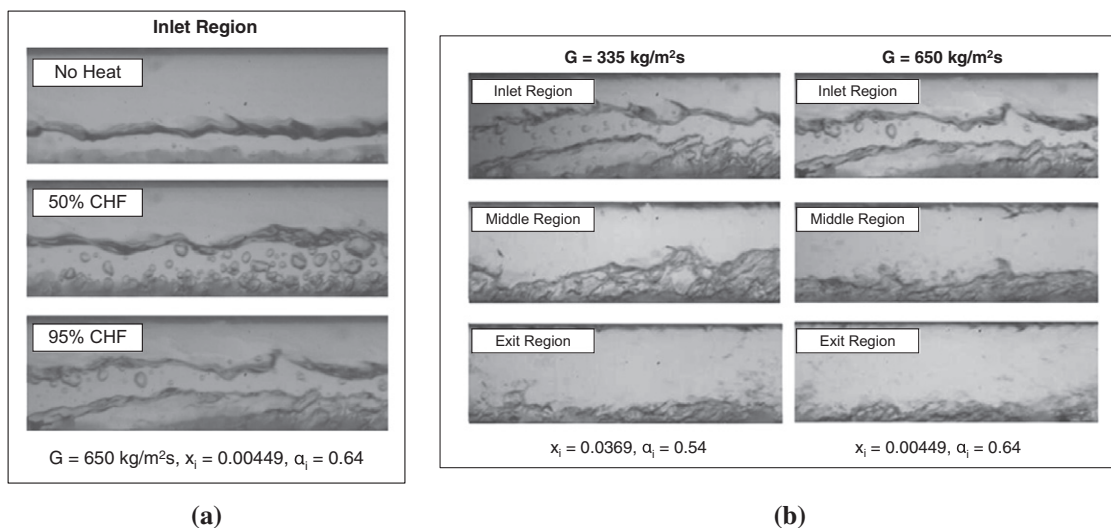


Fig. 4. Images of boiling flow depicting (a) effects of increasing heat flux for inlet region with $G = 650 \text{ kg/m}^2\text{s}$, and (b) variations in boiling behavior with mass velocity for inlet, middle and exit regions at 95% CHF.

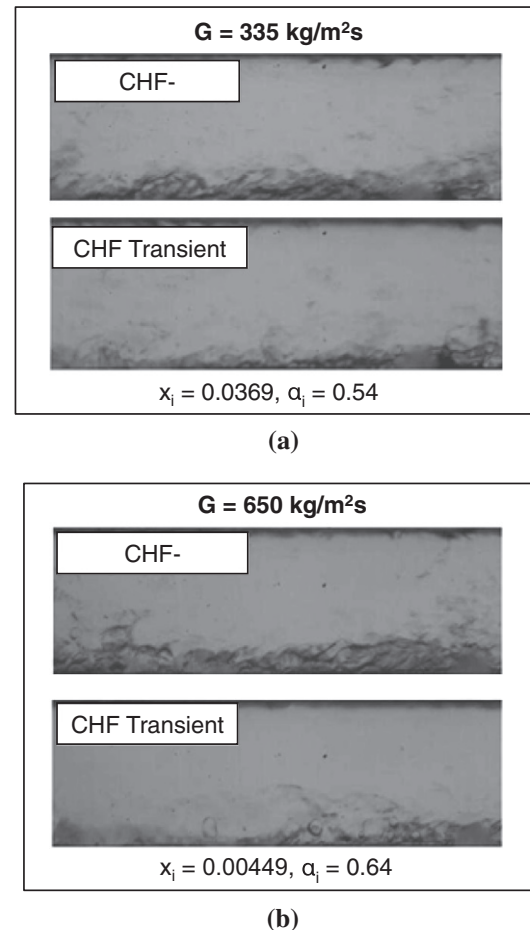


Fig. 5. Images of boiling flow in exit region at CHF- and during CHF transient for (a) $G = 335 \text{ kg/m}^2\text{s}$ and (b) $G = 650 \text{ kg/m}^2\text{s}$.

4. Experimental results

Fig. 6 shows boiling curves for $G = 507$ and $804 \text{ kg/m}^2\text{s}$ measured by the most downstream thermocouple of the heated wall, where CHF was detected first for these two mass velocities. Shown

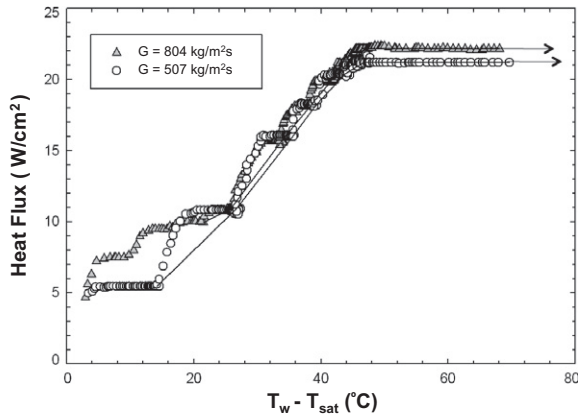


Fig. 6. Boiling curves for $G = 507 \text{ kg/m}^2\text{s}$ ($x_i = 0.05$) and $G = 804 \text{ kg/m}^2\text{s}$ ($x_i = 0.02$).

are both transient and steady state data to illustrate both how the steady-state boiling curve data are reached following each power increment, and the clear wall temperature excursion following the attainment of CHF. Fig. 6 shows the higher mass velocity nets an increase in CHF value.

Fig. 7(a) and (b) show the variation of CHF with inlet quality, x_i , and exit quality, x_o , respectively. A broader range of quality is possible at low mass velocities. Achieving the same quality range is more difficult at higher mass velocities because of an appreciable increase in pressure drop across the flow channel. Both figures show CHF mostly increasing, albeit slightly, with increases in x_i or x_o . Despite the reduced liquid content with increasing quality, this CHF trend can be explained by the higher quality values increasing the liquid velocity. Both figures show the expected trend of CHF increasing with increasing mass velocity.

Void fraction could be measured only for relatively low mass velocities in the range of $G = 185\text{--}790 \text{ kg/m}^2\text{s}$. This is not possible for higher mass velocities because of the aforementioned lack of phase separation. Fig. 7(c) shows the variation of CHF with inlet void fraction, α_i , for different mass velocities. For each mass velocity, CHF generally increases with increasing α_i because of the aforementioned increase in liquid velocity. Fig. 7(d) shows CHF increases monotonically with increasing mass velocity for a given value of exit quality.

Experiments with mass velocities below $340 \text{ kg/m}^2\text{s}$ show differences in interfacial behavior during the CHF transient from those observed with higher mass velocities. First, three clearly separated layers are observed at the inlet to the heated portion of the channel below $340 \text{ kg/m}^2\text{s}$. This behavior is far less obvious at high mass velocities because of the thinning of the vapor wall layer. Second, CHF below $340 \text{ W/m}^2\text{s}$ is initiated at the most upstream thermocouple, while CHF for higher mass commences at the most downstream thermocouple. Fig. 8(a) and (b) show temporal temperature records measured by the five thermocouples embedded along the heated wall during the CHF transient up to and including the instant the electrical power input to the heated wall was cut-off to prevent any physical damage caused by the CHF temperature excursions. In these plots, T_1 denotes the most upstream temperature and T_5 the most downstream. For a low mass velocity of $G = 177.6 \text{ kg/m}^2\text{s}$ ($x_i = 0.1225$), Fig. 8(a) shows CHF is detected first by the most upstream thermocouple T_1 followed by T_2 . On the other hand, Fig. 8(b) shows CHF for a relatively high mass velocity of $G = 1583 \text{ kg/m}^2\text{s}$ ($x_i = 0.0419$) is detected first by the most downstream thermocouple T_5 followed by T_4 .

These transient CHF trends provide valuable insight into the CHF mechanism. Prior studies of flow boiling CHF for zero inlet void conditions show ample evidence that CHF is preceded by

the formation of a wavy vapor layer along the heated wall, which permits liquid access to the wall only in wetting fronts, where the troughs of the wavy vapor layer interface make contact with the wall [7–9,15,26–28]. The same studies show that CHF is triggered by lift-off of a wetting front, preventing liquid access to the wall. With this lift-off, heat from the wall is now concentrated in a fewer number of wetting fronts, which accelerates the lift-off of these wetting fronts as well. Discussed later in this study is how the interfacial lift-off mechanism may explain both the CHF mechanism and differences in the location of CHF commencement.

Fig. 9(a) and (b) show pressure drop measured across the heated wall channel at CHF-. This pressure drop includes a 13-mm region between the upstream pressure tap and upstream edge of the heated wall, and a second 13-mm region between the downstream edge of the heated section and downstream pressure tap. It should be noted that the cross-section of the flow channel is uniform throughout, including both the development flow region upstream of the heated length and the downstream region. Fig. 9(a) shows the pressure drop increases monotonically with increasing mass velocity for a fixed inlet quality. Notice how higher quality values increase pressure drop, which can be explained by both the frictional and accelerational components of pressure drop increasing with increasing quality. Fig. 9(b) shows that increasing inlet void fraction for a fixed mass velocity precipitates a monotonic increase in pressure drop; this increase is more pronounced at higher mass velocities.

5. Separated flow model

A new type of separated flow model is proposed as a foundation for CHF prediction. Fig. 10(a) shows a schematic of horizontal flow with finite inlet void based on conditions observed at CHF-. Because of buoyancy effects, the flow upstream of the heated wall is assumed to consist of a vapor layer residing above a liquid layer. A third vapor layer begins to form at the leading edge of the heated wall, resulting in a separated three-layer flow. The mass flow rate of the lower vapor layer adjacent to the heated wall grows along the heated wall. Slip flow assumptions are adopted in the model, meaning each of the three layers is characterized by a uniform velocity while allowing for differences among velocities of the three layers. Pressure is assumed uniform across the channel's cross-sectional area.

In this model, mass, momentum and energy conservation laws are applied to a control volume of length Δz of the flow channel starting with the upstream edge of the heated wall. The following equations are used to relate flow quality, velocity and void fraction for the top vapor layer of thickness δ_1 , lower vapor layer of thickness δ_2 , and intermediate liquid layer of thickness $H - \delta_1 - \delta_2$, respectively.

$$x_1 = \frac{\rho_g U_{g1} A_{g1}}{GA} = \frac{\rho_g U_{g1} \alpha_1}{G}, \quad (1)$$

$$x_2 = \frac{\rho_g U_{g2} A_{g2}}{GA} = \frac{\rho_g U_{g2} \alpha_2}{G}, \quad (2)$$

and

$$(1 - x_2 - x_2) = \frac{\rho_f U_f A_f}{GA} = \frac{\rho_f U_f (1 - \alpha_1 - \alpha_2)}{G}. \quad (3)$$

Conservation of mass for the combined flow gives

$$\frac{dW}{dz} = 0, \quad (4)$$

which implies both W and G are constant.

Because the entire flow is saturated, there is no temperature gradient between the top vapor layer and middle liquid layer.

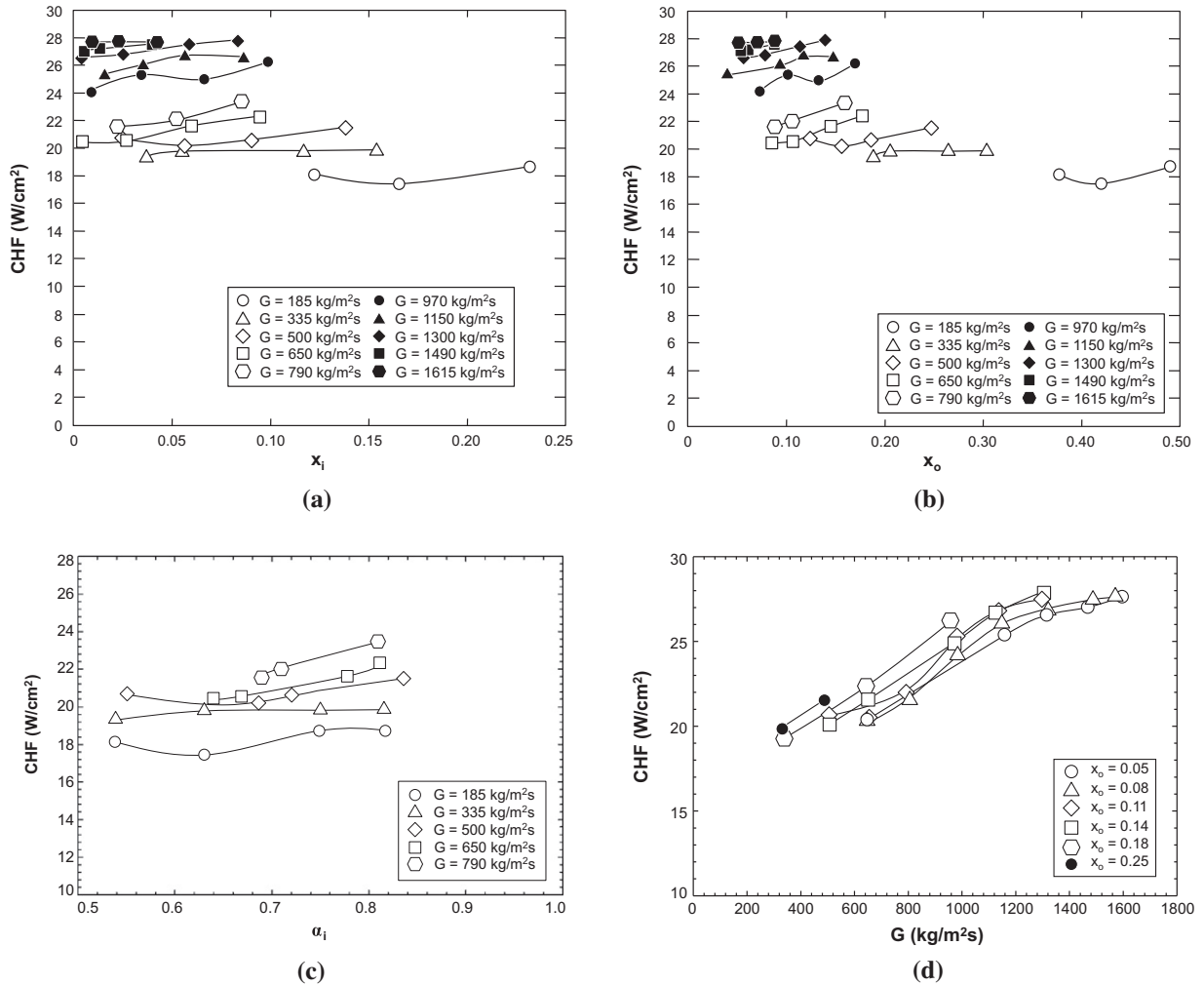


Fig. 7. Variation of CHF with (a) inlet flow quality, (b) exit flow quality, (c) inlet void fraction and (d) mass velocity.

Therefore, any minor mass transfer along the interface is assumed negligible and the mass flow rate of the top vapor layer, x_1W , constant, which implies x_1 is also constant. The growth of the lower vapor layer is accounted for entirely by evaporation of the middle liquid layer. Conservation of mass yields the following relation for the rate of liquid evaporation along the lower vapor–liquid interface.

$$W'_{fg} = GA \frac{dx_2}{dz}. \tag{5}$$

Conservation of momentum for control volumes of length Δz encompassing the top vapor layer, middle liquid layer, and lower vapor layer, yields, respectively,

$$G^2 \frac{d}{dz} \left[\frac{x_1^2}{\rho_g \alpha_1} \right] = -\alpha_1 \frac{dP}{dz} - \frac{\tau_{w,g1} P_{w,g1}}{A} \mp \frac{\tau_{i1} P_{i1}}{A}, \tag{6}$$

$$G^2 \frac{d}{dz} \left[\frac{(1-x_1-x_2)^2}{\rho_f (1-\alpha_1-\alpha_2)} \right] + W'_{fg} u_{i2} = -(1-\alpha_1-\alpha_2) \frac{dP}{dz} - \frac{\tau_{w,f} P_{w,f}}{A} \pm \frac{\tau_{i1} P_{i1}}{A} \pm \frac{\tau_{i2} P_{i2}}{A}, \tag{7}$$

and

$$G^2 \frac{d}{dz} \left[\frac{x_2^2}{\rho_g \alpha_2} \right] - W'_{fg} u_{i2} = -\alpha_2 \frac{dP}{dz} - \frac{\tau_{w,g2} P_{w,g2}}{A} \mp \frac{\tau_{i2} P_{i2}}{A}. \tag{8}$$

In the above equations, P is the pressure, $\tau_{w,g1}$, $\tau_{w,f}$ and $\tau_{w,g2}$ the wall shear stresses for the top vapor layer, middle liquid layer and bottom vapor layer, respectively, $P_{w,g1}$, $P_{w,f}$, and $P_{w,g2}$ the perimeter of the top vapor layer, middle liquid layer and lower vapor layer, respectively, in contact with the channel walls, and P_{i1} and P_{i2} the contact perimeters between the top vapor layer and middle liquid layer and between the middle liquid layer and bottom vapor layer, respectively. The \pm sign in the interfacial shear terms is intended to allow for any variations in the direction of the shear stress, depending on local velocity differences between the three layers. The shear stress direction can be traced on a local basis from numerical solution of Eqs. (6)–(8), combined with mass and energy conservation.

Because the vapor generated at the wall is ejected normal to the wall, it will have no initial stream-wise velocity [9] and, as such, does not contribute stream-wise momentum to the control volume. Therefore, the interfacial momentum terms in Eqs. (7) and (8) are neglected.

Applying the relations $\alpha_1 = \delta_1/H$ and $\alpha_2 = \delta_2/H$ to define friction perimeters, and recalling that $dx_1/dz = 0$, Eqs. (6)–(8) can be expressed, respectively, as

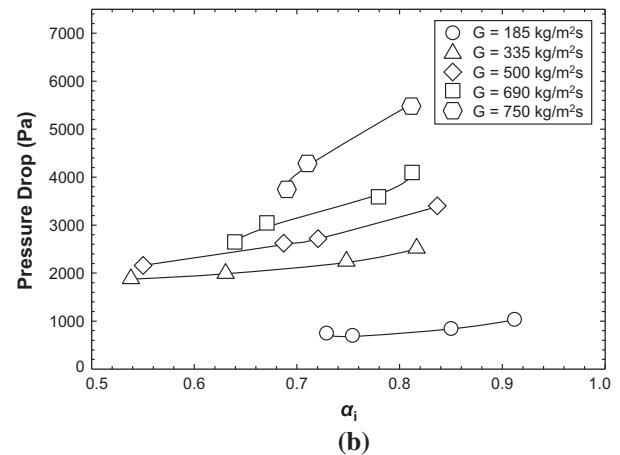
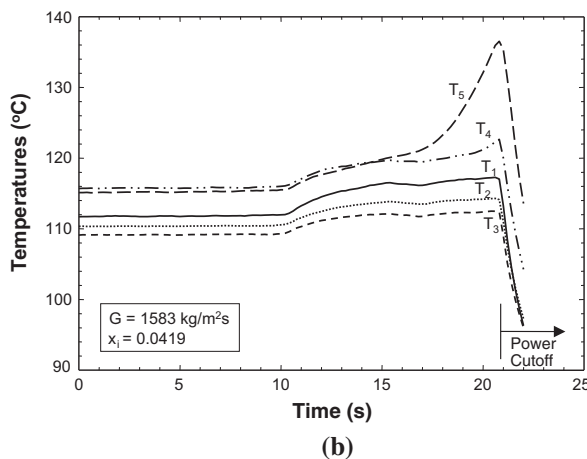
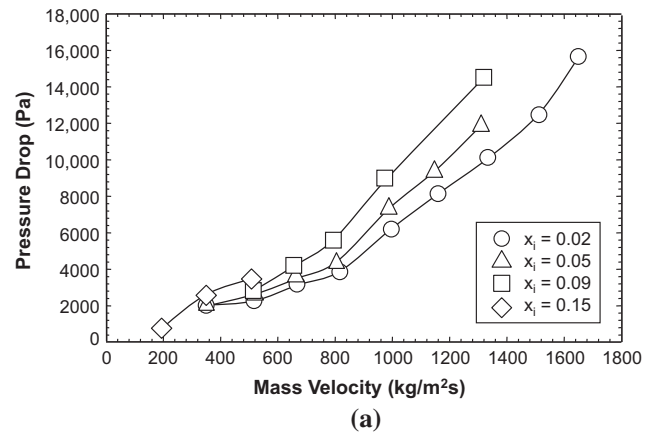
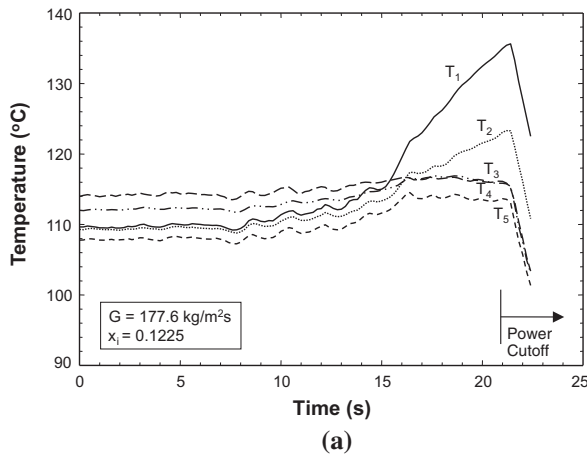


Fig. 8. Temporal records of heated wall thermocouples during CHF transient for (a) $G = 177.6 \text{ kg/m}^2\text{s}$ ($x_i = 0.1225$) and (b) $G = 1583 \text{ kg/m}^2\text{s}$ ($x_i = 0.0419$).

Fig. 9. Variation of measured pressure drop with (a) mass velocity for different inlet qualities, and (b) inlet void fraction for different mass velocities.

$$\frac{G^2}{\rho_g} \left[-\frac{x_1^2}{\alpha_1^2} \frac{d\alpha_1}{dz} \right] - \frac{G^2 x_1^2}{\rho_g^2 \alpha_1} \frac{d\rho_g}{dP} \frac{dP}{dz} = -\alpha_1 \frac{dP}{dz} - \tau_{w,g1} \left[\frac{1}{H} + \frac{2}{w} \alpha_1 \right] \mp \tau_{i1} \frac{1}{H}, \quad (9)$$

$$\frac{G^2}{\rho_f} \left[-\frac{2(1-x_1-x_2)}{(1-\alpha_1-\alpha_2)} \frac{dx_2}{dz} + \frac{(1-x_1-x_2)^2}{(1-\alpha_1-\alpha_2)^2} \frac{d\alpha_1}{dz} + \frac{(1-x_1-x_2)^2}{(1-\alpha_1-\alpha_2)^2} \frac{d\alpha_2}{dz} \right] - \frac{G^2 (1-x_1-x_2)^2}{\rho_f^2 (1-\alpha_1-\alpha_2)} \frac{d\rho_f}{dP} \frac{dP}{dz} = -(1-\alpha_1-\alpha_2) \frac{dP}{dz} - \tau_{w,f} \left[\frac{2}{w} (1-\alpha_1-\alpha_2) \right] \pm \tau_{i1} \frac{1}{H} \pm \tau_{i2} \frac{1}{H} \quad (10)$$

and

$$\frac{G^2}{\rho_g} \left[\frac{2x_2}{\alpha_2} \frac{dx_2}{dz} - \frac{x_2^2}{\alpha_2^2} \frac{d\alpha_2}{dz} \right] - \frac{G^2 x_2^2}{\rho_g^2 \alpha_2} \frac{d\rho_g}{dP} \frac{dP}{dz} = -\alpha_2 \frac{dP}{dz} - \tau_{w,g2} \left[\frac{1}{H} + \frac{2}{w} \alpha_2 \right] \mp \tau_{i2} \frac{1}{H}. \quad (11)$$

The wall shear stress for each phase is defined as

$$\tau_{w,k} = \frac{1}{2} \rho_k U_k^2 f_k, \quad (12)$$

where $k = f$ or g , depending on the phase being modeled. The friction factor in Eq. (12) is obtained from the following relation by Bhatti and Shah [29],

$$f_k = C_1 + \frac{C_2}{Re_{D,k}^{1/C_3}} = C_1 + \frac{C_2}{\left(\frac{\rho_k U_k D_k}{\mu_k} \right)^{1/C_3}}, \quad (13)$$

where $C_1 = 0$, $C_2 = 16$ and $C_3 = 1$ for laminar flow ($Re_{D,k} \leq 2100$), $C_1 = 0.0054$, $C_2 = 2.3 \times 10^{-8}$ and $C_3 = -2/3$ for transitional flow

($2100 < Re_{D,k} \leq 4000$), and $C_1 = 0.00128$, $C_2 = 0.1143$ and $C_3 = 3.2154$ for turbulent flow ($Re_{D,k} > 4000$). The diameter in Eq. (13) is defined as $D_k = 4A_k/P_k = 2H_k w / (H_k + w)$.

The two interfacial shear stresses are determined according to the relations

$$\tau_{i1} = \frac{C_{f,i}}{2} \rho_g (U_{g1} - U_f)^2 \quad (14)$$

and

$$\tau_{i2} = \frac{C_{f,i}}{2} \rho_g (U_{g2} - U_f)^2 \quad (15)$$

where $C_{f,i}$ is the interfacial friction coefficient. Galloway and Mudawar [8] examined several models to determine $C_{f,i}$ and recommended a constant value of 0.5 for a wavy vapor–liquid interface.

Applying energy conservation to a control volume of length Δz encompassing the entire cross-sectional area of the channel yields

$$\frac{dx}{dz} = \frac{dx_2}{dz} = \frac{q'' P_h}{W h_{fg}} = \frac{q'' w}{W h_{fg}}. \quad (16)$$

Eqs. (1)–(3), (9)–(11) and (16) and are solved simultaneously using a fourth-order Runge–Kutta numerical scheme along the channel using saturated properties based on local pressure. This yields values for pressure, qualities, void fractions and velocities of three separated layers for every Δz axial increment from the upstream edge of the heated wall to the downstream edge. The main inputs required for the model, which are defined at the leading edge of the heated wall, are mass velocity, inlet pressure, inlet quality x_i

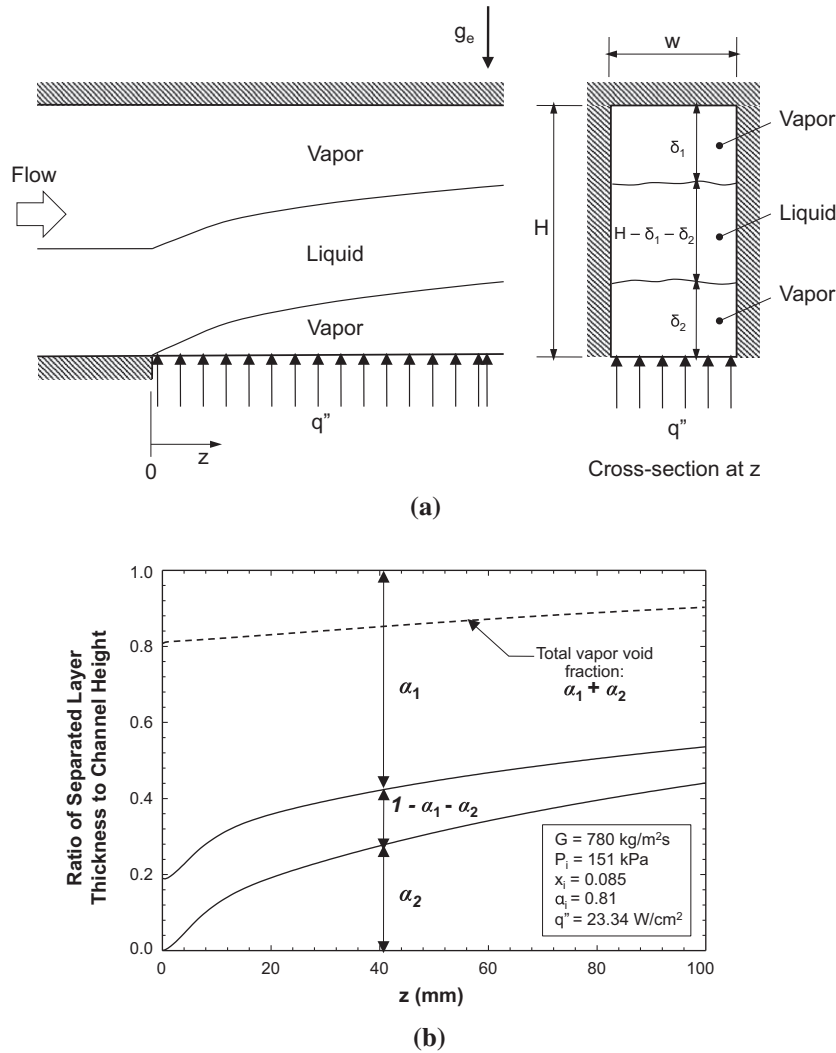


Fig. 10. (a) Schematic of separated three-layer model. (b) Model predictions of void fraction.

(which is equal to inlet vapor quality x_{1i} of the top vapor layer), inlet height δ_{1i} of the top vapor layer, and wall heat flux q'' .

Fig. 10(b) shows thickness variations of the three separated layers along the heated portion of the flow channel for $G = 780 \text{ kg/m}^2\text{s}$, $P_i = 151 \text{ kPa}$, $x_i = 0.085$, $\alpha_i = 0.81$, and $q'' = 23.34 \text{ W/cm}^2$. The thicknesses are represented by void fractions α_1 for the top vapor layer, $1 - \alpha_1 - \alpha_2$ for the middle liquid layer, and α_2 for the lower vapor layer. The model shows the lower layer growing in thickness axially, while the top vapor layer is squeezed along because of the axially increasing shear forces. Also shown in Fig. 10(b) is the total void fraction, $\alpha_1 + \alpha_2$, increasing gradually along the heated length because of the relatively fast thickening of the lower vapor layer.

As discussed earlier in conjunction with the flow visualization results, the separated three-layer behavior is clearly recognizable near in the inlet region of the heated wall, but difficult to track for the middle and exit regions. Recall that the model tackles all the forces acting axially on the control volumes used. The model does not account for the transverse buoyancy forces responsible for any potential downstream mixing between the layers. It can therefore be concluded that the model's greatest value is in predicting interfacial behavior in the upstream region. As shown in Fig. 8(a), this is the region where CHF is detected first for relatively low mass velocities, rendering the model effective at predicting CHF for these conditions. Even for high mass velocities, the

Interfacial Lift-off Model is based on upstream development of the wall vapor layer, which is where the interfacial wavelength is established [9].

The present separated flow model is used to predict pressure drop over a mass velocity range of 185–800 $\text{kg/m}^2\text{s}$. Predictions are compared to experimental data from the present study based on input measured values of G , P_i , x_i , α_i and q'' . As indicated in Table 1, the separated flow model predicts the present data with a mean absolute error of 56.9%, where

$$MAE = \frac{1}{M} \sum \frac{|\Delta P_{\text{pred}} - \Delta P_{\text{exp}}|}{\Delta P_{\text{exp}}} \times 100\% \quad (17)$$

This error can be traced to the aforementioned downstream buoyancy and mixing effects not accounted for in the model. Nonetheless, as discussed later, the greatest value of the model is in predicting the upstream development of the wall vapor layer.

The present pressure drop data are also compared to predictions of the Homogenous Equilibrium Model (HEM). As shown in Table 1, both constant two-phase friction factors [30–34] and two-phase mixture viscosity models [35–41] are used to predict the two-phase frictional pressure gradient. Predictions are provided for two different constant friction factors, $f_{tp} = 0.003$ and 0.005, and seven different two-phase viscosity models. All HEM

Table 1
Comparison of measured pressure drop to predictions of three-layer separated flow model and homogeneous equilibrium model (HEM) using different two-phase friction factors and viscosity models.

Three-layer separated flow model			
MAE = 56.9%			
Homogeneous equilibrium model (HEM)			
$-\left(\frac{dP}{dz}\right) = -\left\{\left(\frac{dP}{dz}\right)_A + \left(\frac{dP}{dz}\right)_F\right\}$			
$-\left(\frac{dP}{dz}\right)_A = G^2 v_{fg} \frac{dx}{dz}$			
$-\left(\frac{dP}{dz}\right)_F = \frac{2}{D_h} f_{tp} v_f G^2 \left(1 + x \frac{v_g}{v_f}\right), D_h = \frac{4A}{P} = \frac{4Hw}{2(H+w)}$			
<i>Constant friction factor method</i>			
Author (s)	Applications	f_{tp}	MAE [%]
Lewis and Robertson [30], and Markson et al. [31]	High pressure steam-water boilers	0.005	54.35
Bottomley [32], Benjamin and Miller [33], and Allen [34]	Low pressure flashing steam-water flows	0.003	72.68
<i>Two-phase mixture viscosity method</i>			
$f_{tp} = 16 Re_{tp}$ for $Re_{tp} < 2000$			
$f_{tp} = 0.079 Re_{tp}^{-0.25}$ for $2000 \leq Re_{tp} < 20,000$			
$f_{tp} = 0.046 Re_{tp}^{-0.2}$ for $Re_{tp} \geq 20,000$			
$Re_{tp} = GD_h/\mu_{tp}$			
Author (s)	Equation		MAE [%]
McAdams et al. [35]	$\frac{1}{\mu_{tp}} = \frac{x}{\mu_g} + \frac{1-x}{\mu_f}$		45.55
Akers et al. [36]	$\mu_{tp} = \left[\frac{\mu_f}{(1-x) + x \left(\frac{\mu_g}{\mu_f}\right)^{0.5}} \right]$		34.53
Cicchitti et al. [37]	$\mu_{tp} = x\mu_g + (1-x)\mu_f$		27.61
Owens [38]	$\mu_{tp} = \mu_f$		25.43
Dukler et al. [39]	$\mu_{tp} = \frac{xv_g\mu_g + (1-x)v_f\mu_f}{xv_g + (1-x)v_f}$		52.40
Beattie and Whalley [40]	$\mu_{tp} = \omega\mu_g + (1-\omega)(1+2.5\omega)\mu_f$ $\omega = \frac{xv_g}{v_f + xv_{fg}}$		40.04
Lin et al. [41]	$\mu_{tp} = \frac{\mu_f\mu_g}{\mu_g + x^{1.4}(\mu_f - \mu_g)}$		37.94

Table 2

Correlations for flow boiling CHF in rectangular and circular channels, and corresponding MAE in predicting present CHF data.

Author (s)	Equation	Comments	MAE [%]
Bowring [42]	$q_m'' = \frac{A + 0.25D_{h,e}G\Delta h_{sub,i}}{C + L}$ $\Delta h_{sub,i} = h_f - h_i, A = \frac{2.317(D_{h,e}Gh_{fg}/4)F_1}{1.0 + 0.0143F_2D_{h,e}^{0.5}G}$ $C = \frac{0.077F_3D_{h,e}G}{1.0 + 0.347F_4(G/1356)^n}$ $n = 2.0 - 0.5P_R, P_R = 0.145P_o, P_o \text{ in MPa}$ $F_1 = \frac{1}{1.917} \left\{ P_R^{18.942} \exp[20.89(1.0 - P_R)] + 0.917 \right\}$ $F_2 = \frac{1.309F_1}{P_R^{1.316} \exp[2.444(1.0 - P_R)] + 0.309}$ $F_3 = \frac{1}{1.667} \left\{ P_R^{17.023} \exp[16.658(1.0 - P_R)] + 0.667 \right\}$ $F_4 = F_3P_R^{1.649}$	<ul style="list-style-type: none"> - Circular channel - Vertical upflow - Uniformly heated 	37.26
Katto [43]	$q_m'' = q_{m0}'' \left(1.0 + K \frac{\Delta h_{sub,i}}{h_{fg}} \right)$ $q_{m01}'' = 0.25(Gh_{fg}) \frac{1}{L/D_{h,e}}$ $q_{m02}'' = C(Gh_{fg}) We_L^{-0.043} \frac{1}{L/D_{h,e}}, We_L = \frac{G^2L}{\sigma\rho_f}$ $q_{m03}'' = 0.15(Gh_{fg}) \left(\frac{\rho_g}{\rho_f} \right)^{0.133} We_L^{-1/3} \frac{1}{1 + 0.0077L/D_{h,e}}$ $q_{m03}'' = 0.26(Gh_{fg}) \left(\frac{\rho_g}{\rho_f} \right)^{0.133} We_L^{-0.433} \frac{(L/D_{h,e})^{0.171}}{1 + 0.0077L/D_{h,e}}$ <p>For $L/D_{h,e} < 50$, $C = 0.25$ For $L/D_{h,e} > 50$, $C = 0.34$ $K_1 = 1$ $K_2 = \frac{0.261}{C We_L^{-0.043}}$ $K_3 = \frac{0.5556(0.0308 + D_{h,e}/L)}{(\rho_g/\rho_f)^{0.133} We_L^{-1/3}}$ When $q_{m01}'' < q_{m02}''$, $q_{m0}'' = q_{m01}''$, $K = K_1$ When $q_{m01}'' > q_{m02}''$, if $q_{m02}'' < q_{m03}''$, $q_{m0}'' = q_{m02}''$, $K = K_2$ If $q_{m02}'' > q_{m03}''$, if $q_{m03}'' < q_{m04}''$, $q_{m0}'' = q_{m03}''$, $K = K_3$ If $q_{m03}'' > q_{m04}''$, $q_{m0}'' = q_{m04}''$</p>	<ul style="list-style-type: none"> - Rectangular channel - Vertical flow <p><u>For water:</u> One-sided heated wall $26 < L/D_{h,e} < 500$ for $P = 3.2 - 13.8$ MPa and $0.417 < L/D_{h,e} < 6.02$ for $P = 101$ kPa <u>For R-113:</u> Two-sided heated walls $L/D_{h,e} = 25$ for $P = 120 - 147$ kPa</p>	55.18
Mishima and Ishii [44]	$q_m'' = \frac{A}{A_h} h_{fg} \left[\left(\frac{1}{C_0} - 0.11 \right) \sqrt{\rho_g g (\rho_f - \rho_g) D_{h,e}} + \frac{\Delta h_{sub,i}}{h_{fg}} G \right]$ <p>For rectangular channels :</p> $C_0 = 1.35 - 0.35 \sqrt{\frac{\rho_g}{\rho_f}}$ <p>For round tubes :</p> $C_0 = 1.2 - 0.2 \sqrt{\frac{\rho_g}{\rho_f}}$	<ul style="list-style-type: none"> - Circular internally heated annulus - Vertical upflow <p><u>For water:</u> $D_i = 0.02045$ m $D_o = 0.02596$ m $L_h = 0.5969$ m $P = 101$ kPa $G = 0 - 600$ kg/m²s $\Delta h_{sub,i} = 160 - 330$ kJ/kg</p>	15.22
Katto and Ohno [45]		<ul style="list-style-type: none"> - Circular channel - Vertical upflow 	26.61

(continued on next page)

Table 2 (continued)

Author (s)	Equation	Comments	MAE [%]
	$q''_m = q''_{m0} \left(1.0 + K \frac{\Delta h_{sub,i}}{h_{fg}} \right)$ $q''_{m01} = C(Gh_{fg})We_L^{-0.043} \frac{1}{L/D_{h,e}}$ $q''_{m02} = 0.1(Gh_{fg}) \left(\frac{\rho_g}{\rho_f} \right)^{0.133} We_L^{-1/3} \frac{1}{1 + 0.0031L/D_{h,e}}$ $q''_{m03} = 0.098(Gh_{fg}) \left(\frac{\rho_g}{\rho_f} \right)^{0.133} We_L^{-0.433} \frac{(L/D_{h,e})^{0.27}}{1 + 0.0031L/D_{h,e}}$ $q''_{m04} = 0.0384(Gh_{fg}) \left(\frac{\rho_g}{\rho_f} \right)^{0.6} We_L^{-0.173} \frac{1}{1 + 0.28We^{-0.233}(L/D_{h,e})}$ $q''_{m05} = 0.234(Gh_{fg}) \left(\frac{\rho_g}{\rho_f} \right)^{0.513} We_L^{-0.433} \frac{(L/D_{h,e})^{0.27}}{1 + 0.0031L/D_{h,e}}$ <p>For $L/D_{h,e} < 50$, $C = 0.25$ For $50 \leq L/D_{h,e} \leq 150$, $C = 0.25 + 0.0009(L/D_{h,e} - 50)$ For $150 < L/D_{h,e}$, $C = 0.34$</p> $K_1 = \frac{0.261}{CWe_L^{-0.043}}$ $K_2 = \frac{0.8333(0.0124 + D_{h,e}/L)}{(\rho_g/\rho_f)^{0.133}We_L^{-1/3}}$ $K_3 = \frac{1.12(1.52We_L^{-0.233} + D_{h,e}/L)}{(\rho_g/\rho_f)^{0.6}We_L^{-0.173}}$ <p>For $\rho_g/\rho_f < 0.15$: When $q''_{m01} < q''_{m02}$, $q''_{m0} = q''_{m01}$ When $q''_{m01} > q''_{m02}$, if $q''_{m02} < q''_{m03}$, $q''_{m0} = q''_{m02}$; if $q''_{m02} > q''_{m03}$, $q''_{m0} = q''_{m03}$ When $K_1 > K_2$, $K = K_1$; when $K_1 < K_2$, $K = K_2$ For $\rho_g/\rho_f > 0.15$: When $q''_{m01} < q''_{m05}$, $q''_{m0} = q''_{m01}$ When $q''_{m01} > q''_{m05}$, if $q''_{m05} > q''_{m04}$, $q''_{m0} = q''_{m05}$; if $q''_{m05} < q''_{m04}$, $q''_{m0} = q''_{m04}$ When $K_1 > K_2$, $K = K_1$; when $K_1 < K_2$, if $K_2 < K_3$, $K = K_2$; if $K_2 > K_3$, $K = K_3$</p>	– Uniformly heated For water: $20 < L/D_{h,e} < 500$ $P = 10\text{--}200$ bar For R-12: $D_{h,e} = 0.01$ m $L = 1$ m $P = 1.96\text{--}3.44$ MPa $G = 120\text{--}2100$ kg/m ² s $\Delta h_{sub,i} = 0.4\text{--}39.9$ kJ/kg	
Sudo et al. [46]	$q''_m = 0.005h_{fg}G^{0.611} \left[\rho_g(\rho_f - \rho_g)g \sqrt{\frac{\sigma}{(\rho_f - \rho_g)g}} \right]^{0.1945}$	– Rectangular channel – Vertical upflow – Two-sided heating For water: $L/D_{h,e} = 170$ $P = 98.1\text{--}196.1$ kPa $G = 0\text{--}600$ kg/m ² s	71.40
Oh and Englert [47]	$q''_m = \frac{A}{P_{h,e}L} h_{fg} \left[0.458 \left(1.0 + \frac{\Delta h_{sub,i}}{h_{fg}} \right) G + 2.412 \sqrt{\lambda \rho_g g (\rho_f - \rho_g)} \right]$ $\lambda = \sqrt{\frac{\sigma}{(\rho_f - \rho_g)g}}$	– Rectangular channel – Vertical upflow – Uniformly heated For water: $P = 20\text{--}85$ kPa $G = 30\text{--}80$ kg/m ² s $\Delta T_{sub,i} = 5\text{--}72^\circ\text{C}$	552.10

methods are shown underpredicting the pressure drop data, with MAEs ranging from 25.43 to 72.68%. With a MAE of 25.43%, the viscosity model by Owens [38] provides the best predictions among all HEM methods, followed by the viscosity model of Cicchitti et al. [37], which has a MAE of 27.61%.

6. CHF predictions

The present CHF data are compared to predictions of both prior empirical correlations [42–47] and the Interfacial Lift-off Model. Table 2 details three correlations that were developed for flow

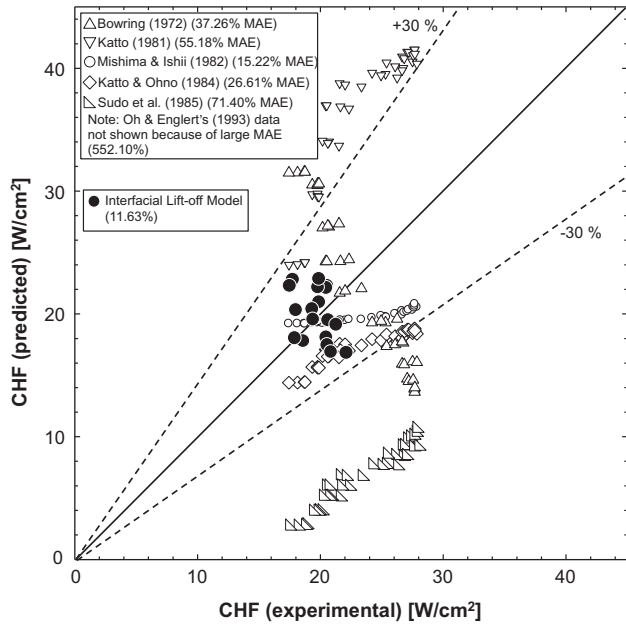


Fig. 11. Comparison of present FC-72 CHF data with predictions of prior CHF correlations and interfacial lift-off model.

boiling CHF in rectangular channels and three other correlations for circular channels. Since some of these correlations are capable of predicting both subcooled and saturated inlet conditions, the subcooling term in these correlations is set to zero when comparing predictions to the present data. Notice that some of these correlations were developed for water alone, others are applicable to other fluids as well.

Notice in Table 2 that the previous CHF correlations are based on different wall heating conditions, some involving heating of only a portion of the circumference, others full circumferential heating. The present rectangular channel configuration involves heating along a heated perimeter equal to one width (w) of the rectangular channel. Therefore, the channel diameter in these correlations is replaced with an equivalent heated diameter defined as

$$D_{h,e} = \frac{4A}{w} = 4H. \quad (18)$$

Fig. 11 compares the predictions of the six correlations to the present data. The accuracy of individual correlations is ascertained using mean absolute error, which is defined as

$$MAE = \frac{1}{M} \sum \frac{|CHF_{pred} - CHF_{exp}|}{CHF_{exp}} \times 100\% \quad (19)$$

With a MAE of 15.22%, Mishima and Ishii's correlation [44] shows the best agreement with the present data. It is followed in accuracy by Katto and Ohno's correlation [45], with a MAE of 26.61%. While Katto's correlation [43] is applicable to rectangular channels, its predictions are inferior to those of Katto and Ohno, with a MAE of 55.18% compared to 26.61%. Despite its moderate MAE of 37.26%, the Bowring correlation [42] does not capture the correct trend of CHF with mass velocity. The correlation by Sudo et al. [46] has a relatively large MAE of 71.40%. The correlation by Oh and Englert [47] is the least accurate of the correlations tested, with MAE of 552.10%. It is important to emphasize that poor predictive capability of a given correlation is not necessarily an assessment of the general accuracy of the correlation, but its unsuitability to the working fluid, flow geometry and operating conditions of the present study.

The present CHF data are also compared to predictions of the Interfacial Lift-off Model. This model has shown remarkable accu-

racy in predicting flow boiling CHF with zero inlet void fraction [7–9,15,26–28]. In the original model, the flow arrives to the heated portion of the channel in saturated or subcooled liquid state, and a wavy vapor layer begins to develop along the heated wall at CHF-. This model is built on the observation that partial wetting of the wall at CHF-is possible only in wetting fronts corresponding to the troughs of the wavy vapor layer interface. CHF is described as the result of lifting of wetting fronts from the wall due to intense vapor effusion. Zhang et al. [15] showed that CHF for zero inlet subcooling can be predicted according to the following relation,

$$q_m'' = b\rho_g h_{fg} \left[\left(\frac{4\pi\sigma\delta}{\rho_g b\lambda_c^2} \sin(b\pi) \right) \Big|_{z_c} \right]^{1/2}, \quad (20)$$

where $b = 0.2$, δ is the thickness of the vapor layer, and λ_c the critical wavelength of instability of the vapor layer interface; both δ and λ_c are calculated at $z^* = z_0 + \lambda_c$ (z^*), where z_0 is the location where the velocity of the vapor layer just exceed that of liquid at the same axial location. The critical wavelength is given by [15]

$$\frac{2\pi}{\lambda_c} = \frac{\rho_f''\rho_g''(U_g - U_f)^2}{2\sigma(\rho_f'' + \rho_g'')} + \sqrt{\left[\frac{\rho_f''\rho_g''(U_g - U_f)^2}{2\sigma(\rho_f'' + \rho_g'')} \right]^2 + \frac{(\rho_f - \rho_g)g}{\sigma}}, \quad (21)$$

where

$$\rho_f'' = \rho_f \coth\left(\frac{2\pi}{\lambda_c} H_f\right), \quad (22)$$

$$\rho_g'' = \rho_g \coth\left(\frac{2\pi}{\lambda_c} H_g\right), \quad (23)$$

and H_f and H_g are the thicknesses of the liquid and vapor layers, respectively. In the original Interfacial Lift-off Model, a two-layer separated flow model is used to determine the axial variations of U_g , U_f and δ , from which the values of δ and λ_c are calculated at z^* to determine CHF according to Eq. (20).

Unlike the original two-layer separated flow for which the original Interfacial Lift-off Model is developed, the present study involves three separated layers because of the finite inlet void fraction. To modify the model to the conditions of the present study, the instability criteria are applied to the interface between the middle liquid layer and bottom vapor layer. Therefore, the vapor layer thickness, δ , in Eq. (20) is substituted by δ_2 , and the vapor velocity, U_g , in Eq. (21) by U_{g2} . Furthermore, because the present separated flow model predicts U_{g2} always exceeding U_f , z_0 is set equal to zero, hence both δ and λ_c in Eq. (20) are evaluated at $z^* = \lambda_c$ (z^*). The mean liquid and vapor layer thicknesses, H_f and H_g , in Eqs. (22) and (23) are given, respectively, by

$$H_f = (1 - \alpha_1 - \alpha_2)H \quad (24)$$

and

$$H_g = \alpha_2 H. \quad (25)$$

Fig. 11 shows the modified Interfacial Lift-off Model is equally successful at predicting CHF for flow boiling in a horizontal channel with finite inlet void fraction, evidenced by a MAE of 11.63%, which is superior to those of the CHF correlations included in the same figure. This demonstrates the validity of the proposed CHF mechanism for the high mass flux conditions that could not be captured with high resolution using video imaging.

7. Conclusions

This study explored saturated flow boiling CHF in a rectangular horizontal channel with an upward-facing heated wall. The influence of inlet vapor void on interfacial behavior at heat fluxes up to CHF as well during the CHF transient was examined with the

aid of high-speed video motion analysis. Based on the observed interfacial behavior, a new model was developed to predict both pressure drop and CHF. Key findings from this study are as follows:

1. With a finite void fraction at the inlet, the flow enters the heated portion of the flow channel clearly separated into two layers, with vapor residing above liquid. A third vapor layer begins to develop at the leading edge of the heated wall beneath the liquid layer. This three-layer behavior is less discernible downstream due to the combined influence of buoyancy and mixing between the separate layers. The three-layer behavior is prevalent for lower mass velocities but less obvious for $G > 790 \text{ kg/m}^2\text{s}$.
2. CHF increases monotonically with increasing mass velocity. CHF also generally increases with increases in inlet quality and inlet void fraction because of increasing liquid velocity caused by flow acceleration.
3. A new separated three-layer model appears to capture the flow behavior in the inlet heated region at CHF-but not the downstream region. Flow behavior in the downstream region is believed to be influenced by buoyancy and mixing effects not accounted for in the model.
4. Overall, good CHF predictions are achieved for all mass velocities by combining the predictions of the separated three-layer model with those of the Interfacial Lift-off Model, evidenced by a MAE of 11.63%.

Acknowledgement

The authors are grateful for the support of the National Aeronautics and Space Administration (NASA) under Grant No. NNX09AJ51A.

References

- [1] I. Mudawar, Two-phase micro-channel heat sinks: theory, applications and limitations, in: Proceedings ASME/JSM 2011 8th Thermal Engineering Conference, Honolulu, HI, March 13–17, Paper No. AJTEC2011-44005, 2011.
- [2] S.S. Kutateladze, A.I. Leont'ev, Some applications of the asymptotic theory of the turbulent boundary layer, in: Proceedings 3rd International Heat Transfer Conference, Chicago, Illinois, vol. 3, 1966, pp. 1–6.
- [3] L.S. Tong, Boundary-layer analysis of the flow boiling crisis, *Int. J. Heat Mass Transfer* 11 (1968) 1208–1211.
- [4] W. Hebel, W. Detavernier, M. Decretion, A contribution to the hydrodynamics of boiling crisis in a forced flow of water, *Nuclear Eng. Design* 64 (1981) 443–445.
- [5] J. Weisman, B.S. Pei, Prediction of critical heat flux in flow boiling at low qualities, *Int. J. Heat Mass Transfer* 26 (1983) 1463–1477.
- [6] C.H. Lee, I. Mudawar, A mechanistic critical heat flux model for subcooled flow boiling based on local bulk flow conditions, *Int. J. Multiphase Flow* 14 (1988) 711–728.
- [7] J.E. Galloway, I. Mudawar, CHF mechanism in flow boiling from a short heated wall-part 1. Examination of near-wall conditions with the aid of photomicrography and high-speed video imaging, *Int. J. Heat Mass Transfer* 36 (1993) 2511–2526.
- [8] J.E. Galloway, I. Mudawar, CHF mechanism in flow boiling from a short heated wall-part 2. Theoretical CHF model, *Int. J. Heat Mass Transfer* 36 (1993) 2527–2540.
- [9] H. Zhang, I. Mudawar, M.M. Hasan, Experimental and theoretical study of orientation effects on flow boiling CHF, *Int. J. Heat Mass Transfer* 45 (2002) 4463–4478.
- [10] H. Zhang, I. Mudawar, M.M. Hasan, Flow boiling CHF in microgravity, *Int. J. Heat Mass Transfer* 48 (2005) 3107–3118.
- [11] H. Zhang, I. Mudawar, M.M. Hasan, Assessment of dimensionless CHF correlations for subcooled flow boiling in microgravity and reduced gravity, *Int. J. Heat Mass Transfer* 50 (2007) 4568–4580.
- [12] D.D. Hall, I. Mudawar, Critical heat flux (CHF) for water flow in tubes-I. Compilation and assessment of world CHF data, *Int. J. Heat Mass Transfer* 43 (2000) 2573–2604.
- [13] D.D. Hall, I. Mudawar, Critical heat flux (CHF) for water flow in tubes-II. Subcooled CHF correlations, *Int. J. Heat Mass Transfer* 43 (2000) 2605–2640.
- [14] D.D. Hall, I. Mudawar, Ultra-high critical heat flux (CHF) for subcooled water flow boiling-II. High-CHF database and design equations, *Int. J. Heat Mass Transfer* 42 (1999) 1429–1456.
- [15] H. Zhang, I. Mudawar, M.M. Hasan, CHF model for subcooled flow boiling in Earth gravity and microgravity, *Int. J. Heat Mass Transfer* 50 (2007) 4039–4051.
- [16] G. Wallis, *One-Dimensional Two-Phase Flow*, McGraw-Hill, New York, 1969.
- [17] J.G. Collier, J.R. Thome, *Convective Boiling and Condensation*, 3rd ed., Clarendon Press, Oxford, UK, 1994.
- [18] R.W. Lockhart, R.C. Martinelli, Proposed correlation of data for isothermal two-phase two-component flow in pipes, *Chem. Eng. Prog.* 45 (1949) 39–48.
- [19] R.C. Martinelli, D.B. Nelson, Prediction of pressure drop during forced circulation boiling of water, *Trans. ASME* 70 (1948) 695–702.
- [20] J.R.S. Thom, Prediction of pressure drop during forced circulation boiling of water, *Int. J. Heat Mass Transfer* 7 (1964) 709–724.
- [21] C.J. Baroczi, A systematic correlation for two-phase pressure drop, in: 8th National Heat Transfer Conference, AIChE paper no. 37, Los Angeles, CA, 1965.
- [22] D. Chisholm, A theoretical basis for the Lockhart–Martinelli correlation for two-phase flow, *Int. J. Heat Mass Transfer* 10 (1967) 1767–1778.
- [23] L. Friedel, Improved friction pressure drop correlations for horizontal and vertical two-phase pipe flow, in: Proceedings European Two-Phase Flow Group Meeting, Paper E2, Ispra, Italy, 1979.
- [24] C.O. Cersey, I. Mudawar, Effects of heater length and orientation on the trigger mechanism for near-saturated flow boiling critical heat flux-I. Photographic study and statistical characterization of the near-wall interfacial features, *Int. J. Heat Mass Transfer* 38 (1995) 629–641.
- [25] C.O. Cersey, I. Mudawar, Effects of heater length and orientation on the trigger mechanism for near-saturated flow boiling critical heat flux-II. Critical heat flux model, *Int. J. Heat Mass Transfer* 38 (1995) 643–654.
- [26] J.C. Sturgis, I. Mudawar, Critical heat flux in a long, rectangular channel subjected to onesided heating – I. Flow visualization, *Int. J. Heat Mass Transfer* 42 (1999) 1835–1847.
- [27] J.C. Sturgis, I. Mudawar, Critical heat flux in a long, rectangular channel subjected to onesided heating-II. Analysis of critical heat flux data, *Int. J. Heat Mass Transfer* 42 (1999) 1849–1862.
- [28] I. Mudawar, A.H. Howard, C.O. Cersey, An analytical model for near-saturated pool boiling CHF on vertical surfaces, *Int. J. Heat Mass Transfer* 40 (1997) 2327–2339.
- [29] M.S. Bhatti, R.K. Shah, Turbulent and transitional convective heat transfer in ducts, in: S. Kakac, R.K. Shah, W. Aung (Eds.), *Handbook of single-phase convective heat transfer*, John Wiley and Sons, New York, 1987.
- [30] W.Y. Lewis, S.A. Robertson, The circulation of water and steam in water-tube boilers and the rational simplification of boiler design, *Proc. Inst. Mech. Eng.* 143 (1940) 147–181.
- [31] A.A. Markson, T. Raverse, C.G.R. Humphreys, A method for estimating the circulation in steam boiler furnace circuits, *Trans. ASME* 64 (1942) 275–286.
- [32] W.T. Bottomley, Flow of boiling water through orifices and pipes, *Trans. North East Coast Inst. Eng. Ship Builders* 53 (1936) 65–100.
- [33] N.W. Benjamin, J.G. Miller, The flow of a flashing mixture of water and steam through pipes, *Trans. ASME* 64 (1942) 657–664.
- [34] W.F. Allen, Flow of a flashing mixture of water and steam through pipes and valves, *Trans. ASME* 73 (1951) 257–265.
- [35] W.H. McAdams, W.K. Woods, L.C. Heroman, Vaporization inside horizontal tubes, II. Benzene-oil mixture, *Trans. ASME* 64 (1942) 193–200.
- [36] W.W. Akers, H.A. Deans, O.K. Crosser, Condensing heat transfer within horizontal tubes, *Chem. Eng. Prog.* 54 (1958) 89–90.
- [37] A. Cicchitti, C. Lombardi, M. Silvestri, G. Soldaini, R. Zavalluilli, Two-phase cooling experiments-pressure drop, heat transfer and burnout measurements, *Energia nucleare* 7 (1960) 407–425.
- [38] W.L. Owens, Two-phase pressure gradient, Part II, *Int. Dev. Heat Trans.* (1961) 363–368. ASME paper no. 41.
- [39] A.E. Dukler, M. Wicks, R.G. Cleaveland, Pressure drop and hold up in two-phase flow, *AIChE J.* 10 (1964) 38–51.
- [40] D.R.H. Beattie, P.B. Whalley, A simple two-phase frictional pressure drop calculation method, *Int. J. Multiphase Flow* 8 (1982) 83–87.
- [41] S. Lin, C.C.K. Kwok, R.Y. Li, Z.H. Chen, Z.Y. Chen, Local frictional pressure drop during vaporization of R-12 through capillary tubes, *Int. J. Multiphase Flow* 17 (1991) 95–102.
- [42] R.W. Bowring, A simple but accurate round tube uniform heat flux, dryout correlation over the pressure range 0.7–17 MN/m² (100–2500 psia), AEEW-R 789, United Kingdom Atomic Energy Authority, 1972.
- [43] Y. Katto, General features of CHF of forced convection boiling in uniformly heated rectangular channels, *Int. J. Heat Mass Transfer* 24 (1981) 1413–1419.
- [44] K. Mishima, M. Ishii, Critical heat flux experiments under low flow conditions in a vertical annulus, ANL-82-6, NUREG/CR-2647, 1982.
- [45] Y. Katto, H. Ohno, An improved version of the generalized correlation of critical heat flux for the forced convective boiling in uniformly heated vertical tubes, *Int. J. Heat Mass Transfer* 27 (1984) 1641–1648.
- [46] Y. Sudo, K. Miyata, H. Ikawa, M. Kaminaga, M. Ohkawara, Experimental study of differences in DNB heat flux between up flow and down flow in vertical rectangular channel, *J. Nucl. Sci. Tech.* 22 (1985) 604–618.
- [47] C.H. Oh, S.B. Englert, Critical heat flux for low flow boiling in vertical uniformly heated thin rectangular channels, *Int. J. Heat Mass Transfer* 36 (1993) 325–335.